SCIENTIFIC REPORTS

OPEN

Work Function Tuning in Two-Dimensional MoS$_2$ Field-Effect-Transistors with Graphene and Titanium Source-Drain Contacts

Seung Su Baik[1], Seongil Im[2] & Hyoung Joon Choi[2,3]

Based on the first principles calculation, we investigate the electronic band structures of graphene-MoS$_2$ and Ti-MoS$_2$ heterojunctions under gate-voltages. By simultaneous control of external electric fields and carrier charging concentrations, we show that the graphene's Dirac point position inside the MoS$_2$ bandgap is easily modulated with respect to the co-varying Fermi level, while keeping the graphene's linear band structure around the Dirac point. The easy modulation of graphene bands is not confined to the special cases where the conduction-band-minimum point of MoS$_2$ and the Dirac point of graphene are matched up in reciprocal space, but is generalized to their dislocated cases. This flexibility caused by the strong decoupling between graphene and MoS$_2$ bands enhances the gate-controlled switching performance in MoS$_2$-graphene hybrid stacking-device.

Molybdenum disulfide (MoS$_2$)[1,2] and graphene[3,4] are rapidly emerging and already successfully emerged nanoelectronic materials. In many ways, MoS$_2$ is compared with its predecessor graphene for their beneficial properties such as outstanding carrier mobility[5–10], high structural flexibility[3,11], and bandgap modulation under external perturbations[12–19]. However, in contrast to gapless graphene, pristine MoS$_2$ shows a sizable bandgap of ~1.3 eV in its bulk state, which further increases up to ~1.9 eV upon exfoliating. For this reason, extensive efforts have been carried out to take advantages from each material and combine them into a single device. Prominent accomplishments in such efforts are the synthesis of stacked graphene-MoS$_2$ junctions[20–23] and their application to field effect transistors (FETs)[24–39] in which MoS$_2$ and graphene are used as a channel and source(S)-drain(D) electrodes, respectively.

In FETs, an ohmic contact is usually desired for easy current flows between semiconductor and S/D electrodes. To fulfill this requirement, relevant contact searching is primarily focused on avoiding materials with the rectifying responses to forward and backward biases. Reported S/D electrodes on MoS$_2$ channel are pure metals such as Ti[5,6,8,40–44], Au[40,45–50], and Sc[42,43], and the most popular material amongst them tends to become Au/Ti deposition followed by a post-annealing process[44]. This choice follows from a prior estimation based on the Schottky-Mott rule[51–53], which states that the potential barrier height at the interface is given by the energy difference between the semiconductor electron affinity and the metal work function. Because the electron affinity of MoS$_2$ is reported as 4.0 eV and the work functions of graphene and Ti are known as 4.5 and 4.3 eV, respectively, MoS$_2$-Ti contact is expected to form a smaller Schottky barrier, leading to a more ohmic behavior. Contrary to this expectation, however, graphene-contacted MoS$_2$ shows higher on-current and lower off-state behaviors, displaying an on/off ratio over ~7.5 × 10^6 [29]. To understand this seemingly anomalous feature, we first constructed graphene/MoS$_2$ and Ti/MoS$_2$ stacking structures, and investigated their electronic band structures by using the first-principles density functional method[54]. In this work, we explicitly show the absence of graphene-induced gap-states, which otherwise would cause a Fermi level (E$_F$) pinning[55] within the bandgap. We then attribute the sensitive variations of E$_F$ and work function under gate-voltages to the strong decoupling between graphene and MoS$_2$ bands in their heterojunction.

[1]School of Computational Sciences, Korea Institute for Advanced Study, Seoul 02455, Korea. [2]Department of Physics and IPAP, Yonsei University, Seoul 03722, Korea. [3]Center for Computational Studies of Advanced Electronic Material Properties, Yonsei University, Seoul 03722, Korea. Correspondence and requests for materials should be addressed to S.S.B. (email: ssbaik@kias.re.kr) or H.J.C. (email: h.j.choi@yonsei.ac.kr)
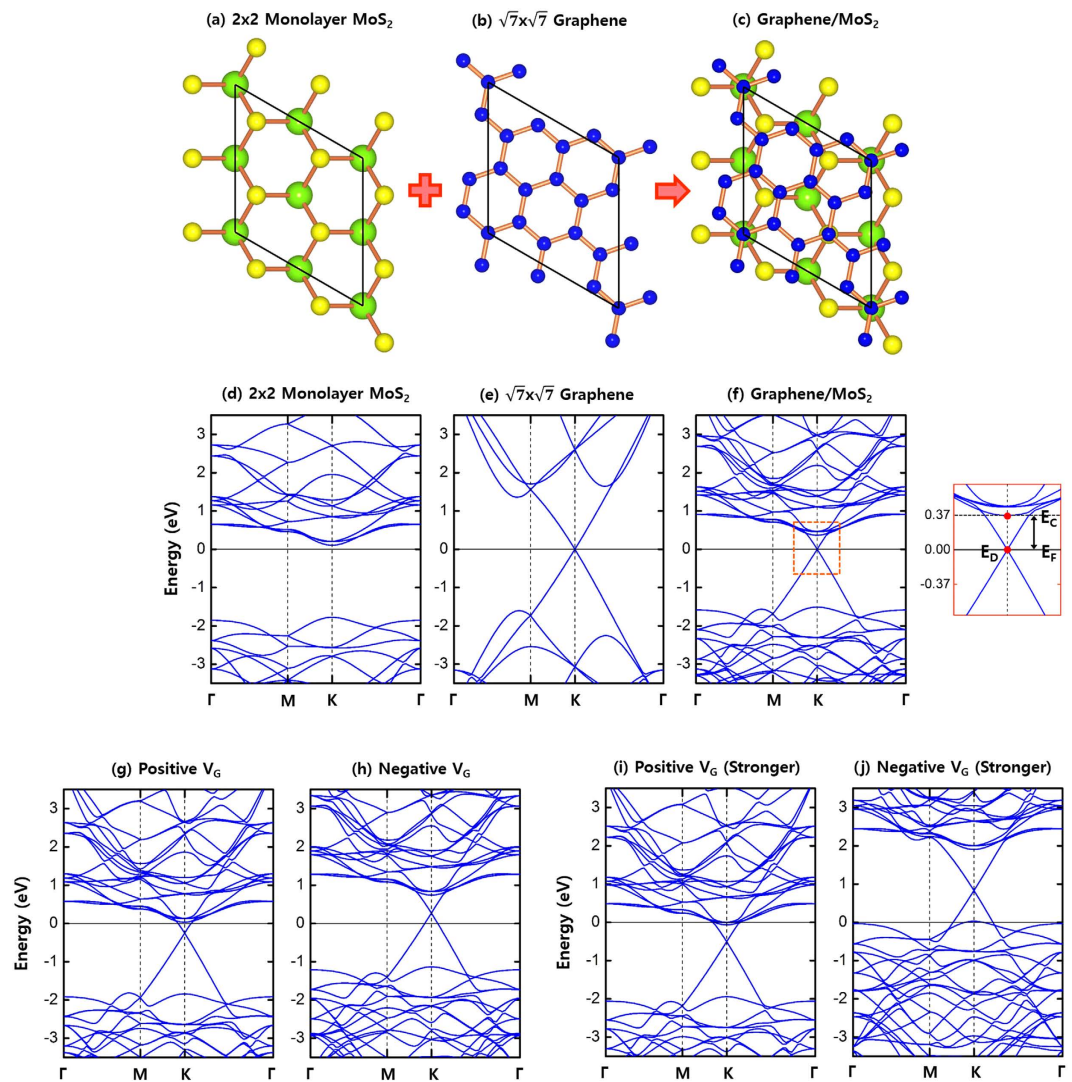
Figure 1. Atomic views and electronic band structures. Top-views of (**a**) 2×2 MoS$_2$ monolayer, (**b**) $\sqrt{7} \times \sqrt{7}$ graphene monolayer, and (**c**) $\sqrt{7} \times \sqrt{7}$-graphene/2×2-MoS$_2$ heterostructure. Green, yellow, and blue spheres represent Mo, S, and C atoms, respectively. Band structures of (**d**) 2×2 MoS$_2$ monolayer, (**e**) $\sqrt{7} \times \sqrt{7}$ graphene monolayer, and (**f**) $\sqrt{7} \times \sqrt{7}$-graphene/2×2-MoS$_2$. Inside the box (orange line), E$_C$, E$_D$, and E$_F$ represent the CBM energy of MoS$_2$, the Dirac point energy of graphene, and the Fermi level of the whole system, respectively. Band structures of $\sqrt{7} \times \sqrt{7}$-graphene/2×2-MoS$_2$ under (**g**) a positive gate-voltage ($E = +0.01$ V/Å and $n_c = 8.7 \times 10^{12}$ cm^{-2}), (**h**) a negative gate-voltage ($E = -0.01$ V/Å and $n_c = -8.7 \times 10^{12}$ cm^{-2}), (**i**) a stronger positive gate-voltage ($E = +0.1$ V/Å and $n_c = 8.7 \times 10^{13}$ cm^{-2}), and (**j**) a stronger negative gate-voltage ($E = -0.1$ V/Å and $n_c = -8.7 \times 10^{13}$ cm^{-2}). The direction of a positive electric field is from MoS$_2$ to graphene.

Computational Methods

To investigate the gate-voltage tuning effects on the graphene(S/D)-MoS$_2$ and Ti(S/D)-MoS$_2$ FETs, we have performed self-consistent density functional calculations using the SIESTA code[54]. Exchange and correlation were treated with the local density approximation (LDA)[56]. Core electrons were replaced by standard norm-conserving pseudo-potentials[57] as transformed into fully nonlocal Kleinman-Bylander form[58]. Valence states were described by numerical atomic orbitals of double-ζ plus polarization basis-set to account for the deformation density induced by bond formations. Electronic wavefunctions and charge densities were projected onto a real space grid with an equivalent energy cutoff of 500 Ry. We used 24×24 k-grid sampling in the full Brillouin zone (BZ) for the slab systems. To describe naturally n-doped MoS$_2$, we performed the virtual crystal approximation (VCA) by replacing 1.3×10^{-4} atomic % of sulfur atoms with chlorine atoms. This corresponds to 5.0×10^{16} cm^{-3} electron doping in bulk MoS$_2$ as consistent with experimental observations[40,59–62]. After the VCA, additional electron charging effects under gate-voltages were simulated by direct electron addition or subtraction methods. For the graphene stacking on MoS$_2$, we considered two different heterostructures with commensurability conditions: (*i*) $\sqrt{7} \times \sqrt{7}$ graphene sheet (6.51 Å) was stacked on 2×2 MoS$_2$ monolayer (6.32 Å) which includes 2.9% lattice contraction of graphene. (*ii*) 4×4 graphene sheet (9.84 Å) was adjusted to 3×3 MoS$_2$ monolayer (9.48 Å),
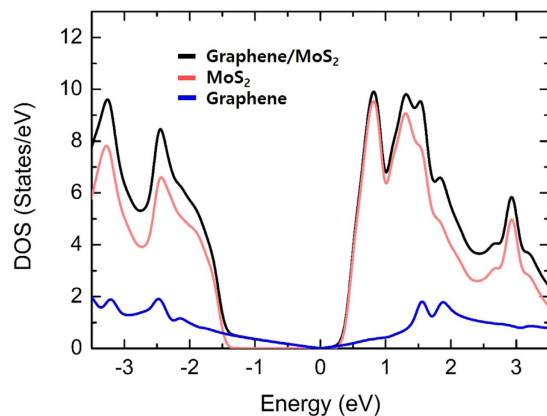
Figure 2. Total and partial density of states (DOS) of $\sqrt{7} \times \sqrt{7}$-graphene/2 × 2-MoS2 system. Black line is the total DOS of the graphene/MoS$_2$ system. Pink line is the partial DOS of MoS$_2$ in the graphene/MoS$_2$ system. Blue line is the partial DOS of graphene in the graphene/MoS$_2$ system.

ΔE (eV)	Ungated	Positive V_G	Negative V_G
$E_C - E_D$	0.37	0.29	0.47
$E_C - E_F$	0.37	0.03	0.74
$E_F - E_D$	0.00	0.25	−0.27

Table 1. Work function variations in positive and negative gate-voltages (V_G) in graphene/MoS$_2$. V_G variations are simulated with the external electric field of $E = \pm 0.01$ V/Å and the electron charging concentration of $\pm 8.7 \times 10^{12}$ cm^{-2}, which corresponds to ± 0.03 electron charging in the $\sqrt{7} \times \sqrt{7}$ -graphene/2 × 2-MoS$_2$ supercell. E_C, E_D, and E_F represent the CBM energy of MoS$_2$, the Dirac point energy of graphene, and the Fermi level of the whole system, respectively.

resulting in 3.7% lattice contraction of graphene. For the Ti stacking on MoS$_2$, 4-layered Ti lattice (a = 2.95 Å) was placed on 1 × 1 MoS$_2$ monolayer (3.16 Å) which includes 6.7% lattice expansion of Ti.

Results and Discussion

In FETs, gate-voltage (V_G) always puts into effects of electron charging and electric field variation in a simultaneous way. Once the system reaches a given state of on-current at a specific positive gate-voltage, both direction and strength of current flows are controlled by the drain-voltage (V_D). Figure 1(f) and (g) show the approaching steps from an ungated case to an on-current stage in $\sqrt{7} \times \sqrt{7}$-graphene/2 × 2-MoS$_2$ heterojuncion. To describe a weak positive (negative) gate-voltage, we have set the external electric field as $E = \pm 0.01$ V/Å and the electron charging concentration as $n_c = \pm 8.7 \times 10^{12}$ cm^{-2}. Here the positive and the negative sign represent the positive and the negative V_G, respectively. To describe stronger gate-voltages, we have increased the electric field and the electron charging concentration by 10 times.

In graphene/MoS$_2$ systems, the Schottky barrier height is defined as the energy difference between the conduction band minimum (CBM) energy (E_C) of MoS$_2$ in the graphene/MoS$_2$ system and the Fermi level (E_F) of the whole system. As seen in Table 1, the Schottky barrier ($\Delta E = E_C - E_F$) in graphene/MoS$_2$ sensitively responds to gate-voltages by decreasing from 0.37 eV (ungated) to 0.03 eV (on-current) in the positive V_G, and by increasing from 0.37 eV (ungated) to 0.74 eV (off-state) in the negative V_G. Easily reducible Schottky barrier in positive V_G means easily diminishable contact resistance[33–37] between graphene and MoS$_2$, which induces large current flows in drain-voltages. In contrast, a large Schottky barrier in negative V_G reduces the unprofitable current leakage in off-states and contributes to the high on/off ratio in itself. The working principles of V_D and V_G are similar to each other, except that V_D additionally controls the chemical potential of graphene with respect to that of MoS$_2$. Thus, the high sensitivity to gate-voltages involves a similar sensitivity to drain-voltages, resulting in a fast slope increase in the I_D-V_D curve and a corresponding high on/off ratio. Meanwhile, as evaluated in Table 1, the system response to gate-voltages is not completely symmetric due to the shape-change of the Dirac cone caused by the electric field. In the positive V_G, the Fermi velocity near the Dirac point decreases from 8.38×10^5 m/s to 8.18×10^5 m/s, and the Dirac point position becomes closer to the CBM energy of MoS$_2$. In contrast, in the negative V_G, the Fermi velocity increases from 8.38×10^5 m/s to 8.45×10^5 m/s, and the Dirac point position becomes far away from the CBM energy of MoS$_2$.

The energy difference between the CBM and the Dirac point ($E_C - E_D$) is decreased by 0.08 eV from the ungated case (0.37 eV) to the positive V_G (0.29 eV), and increased by 0.10 eV from the ungated case (0.37 eV) to the negative V_G (0.47 eV). This slightly asymmetric response can be assured by the energy difference between the Fermi level and the Dirac point ($E_F - E_D$); increment by 0.25 eV from the ungated case to the positive V_G, and decrement by 0.27 eV from the ungated case to the negative V_G. As the gate-voltages increase more, the asymmetry increases further. Shown in Fig. 1(i) and (j) are the band offsets under the strong positive and negative
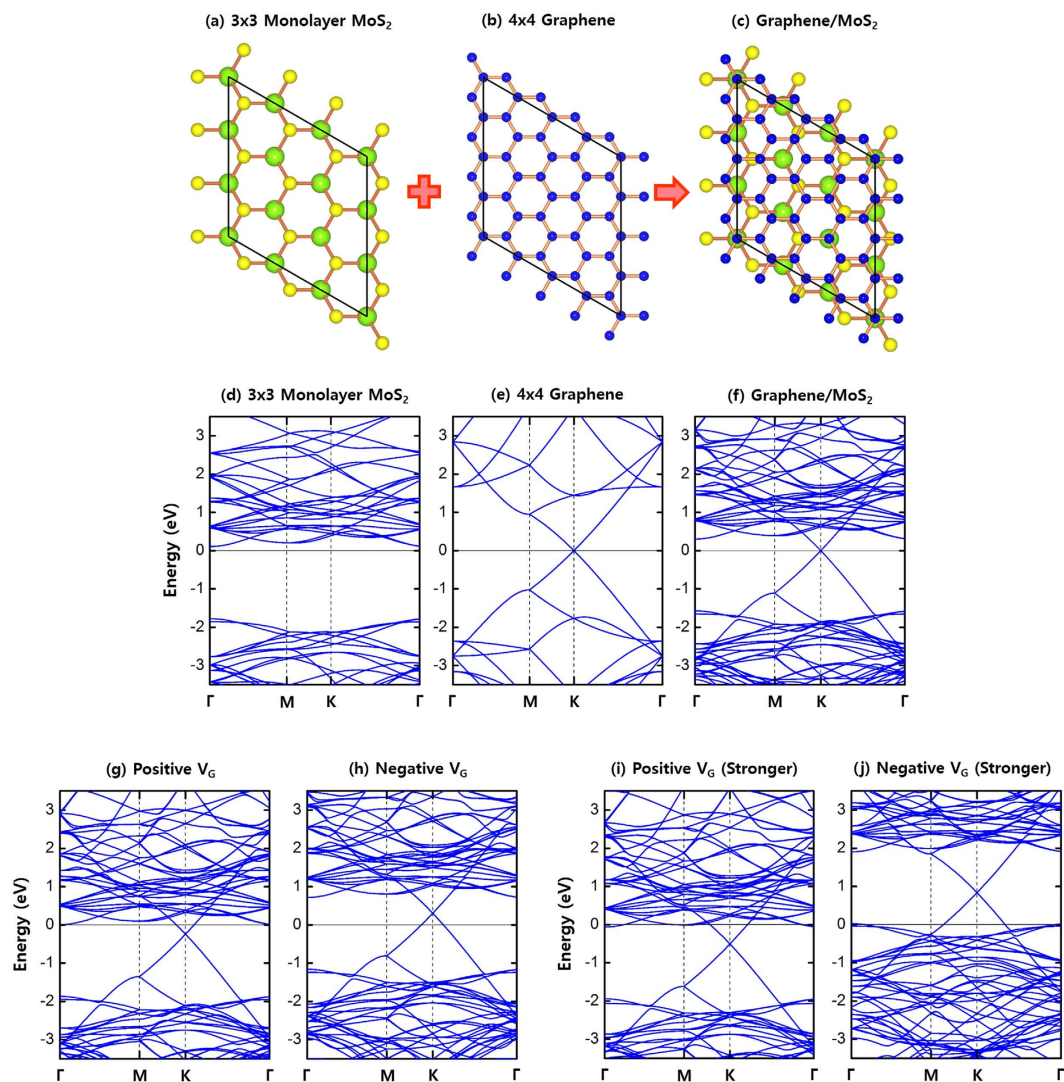
Figure 3. Atomic views and electronic band structures. Top-views of (**a**) 3×3 MoS_2 monolayer, (**b**) 4×4 graphene monolayer, and (**c**) 4×4-graphene/3×3-MoS_2 heterostructure. Green, yellow, and blue spheres represent Mo, S, and C atoms, respectively. Band structures of (**d**) 3×3 MoS_2 monolayer, (**e**) 4×4 graphene monolayer, and (**f**) 4×4-graphene/3×3-MoS_2 heterostructure. Band structures of 4×4-graphene/3×3-MoS_2 heterostructure under (**g**) a positive gate-voltage ($E = +0.01$ V/Å and $n_c = 8.7 \times 10^{12}$ cm^{-2}), (**h**) a negative gate-voltage ($E = -0.01$ V/Å and $n_c = -8.7 \times 10^{12}$ cm^{-2}), (**i**) a stronger positive gate-voltage ($E = +0.1$ V/Å and $n_c = 8.7 \times 10^{13}$ cm^{-2}), and (**j**) a stronger negative gate-voltage ($E = -0.1$ V/Å and $n_c = -8.7 \times 10^{13}$ cm^{-2}). The direction of a positive electric field is from MoS_2 to graphene.

gate-voltages ($E = \pm 0.1$ V/Å and $n_c = \pm 8.7 \times 10^{13}$ cm^{-2}). Intriguingly, Fig. 1(j) shows a theoretical possibility that the conduction type of real systems may transform from electrons to holes under a strong enough negative V_G.

The band structures shown in Fig. 1(d–j) provide two key features on the flexibility of graphene bands: (*i*) We clearly see the absence of graphene-induced gap-states inside the MoS_2 bandgap, which would have a flat-band form in k-space and absorb electrons from metals on stacking. This failure in forming the gap-states unlocks the Fermi level pinning and preferably makes the graphene bands flexible. As shown in Fig. 2, the absence of graphene-induced gap-states is confirmed by the clean density of states (DOS) without extra peaks near the Fermi level. (*ii*) The linear shape of graphene bands around the Dirac point remains intact and the linearity extends over one electron-volt from the Dirac point with a negligible band mixing between graphene and MoS_2. This weak interaction is evidenced from the relatively small binding energy of -0.59 eV and the large equilibrium distance of ~3.23 Å between MoS_2 and graphene[24,25]. In another way, positive electric fields play a role of shifting up the Dirac point toward a higher energy, so if we increase the electric field over ~0.5 V/Å without the electron charging, the Dirac point moves up above the CBM, making the conical vicinity of the Dirac point empty, which then forces E_F to be located above the CBM to compensate this charge depletion. Even in this extreme electric field, the linearity is retained around the Dirac point, indicating the strong decoupling between graphene and MoS_2 bands.

Thus far, all analyses were performed for the case with the CBM of MoS_2 and the Dirac point of graphene coincided at the special k-point K. To extend the validity to more general cases where the CBM point and the Dirac
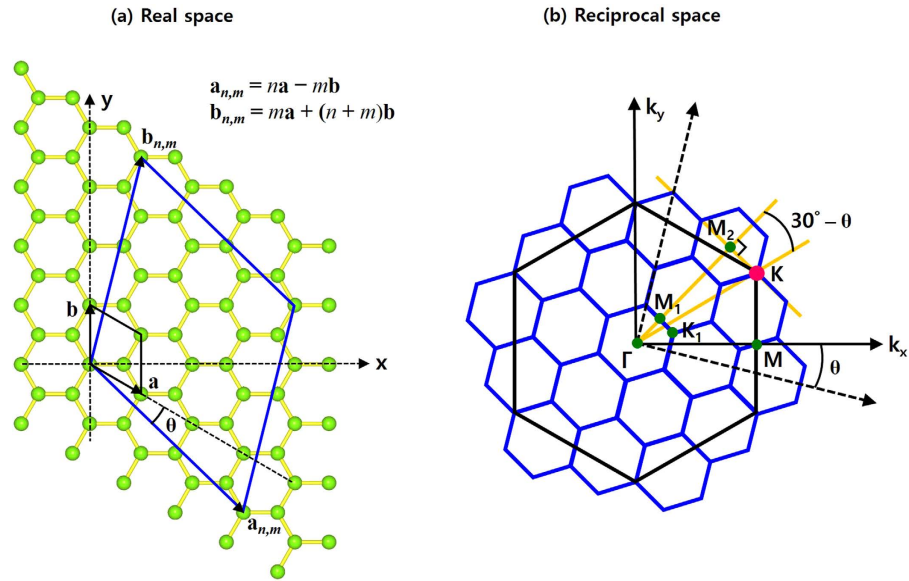
Figure 4. Mapping of special k-points. (**a**) Lattice vectors of a general hexagonal supercell in real space. $a_{m,n} = ma - nb$ and $b_{m,n} = na + (m+n)b$, where a and b are the lattice vectors of 1×1 hexagonal unit cell: $a = \frac{\sqrt{3}}{2}\hat{x} - \frac{1}{2}\hat{y}$ and $b = \hat{y}$. (**b**) Location of special k-points in reciprocal space. The geometric condition $\overline{M_1K_1} \cdot N_s = \overline{M_2K}$ gives rise to the integer value of $N_s = \frac{2}{\sqrt{3}}\alpha \cos\left(\frac{\pi}{6} - \theta\right) = n - m$, where $\alpha = \sqrt{n^2 + nm + m^2}$. If N_s is a multiple of three, the K point of the unit cell Brillouin zone (BZ) coincides with the Γ point of the supercell BZ. Otherwise, it coincides with the K point of the supercell BZ.

point are mismatched, we consider the supercells of 4×4 graphene stacked on 3×3 MoS$_2$. In this new stacking, the CBM point is moved to Γ whereas the Dirac point is still located at K as shown in Fig. 3. We see that all features previously analyzed in Fig. 1 are similarly exhibited in Fig. 3. The band lineups in 4×4-graphene/3×3-MoS$_2$ reproduce sensitive and asymmetric responses to gate-voltages. Also, we see that graphene-induced gap-states do not appear, and the linear dispersion around the Dirac point remains intact on stacking and in onward applications of gate-voltages, leading to the strong decoupling between graphene and MoS$_2$ bands. Thus, Fig. 3 confirms that the flexibility of graphene bands is not confined to the special cases where the CBM and Dirac points are matched up in reciprocal space, but is generalized to their dislocated cases.

Before going to Ti stacking on MoS$_2$, we here analyze the position movement of special k-points from the 1×1 hexagonal unit cell to a general hexagonal supercell. Figure 4(a) shows the general hexagonal lattice in real space. The supercell lattice vectors (blue lines) are expressed as $a_{m,n} = ma - nb$ and $b_{m,n} = na + (m+n)b$, where $a = \frac{\sqrt{3}}{2}\hat{x} - \frac{1}{2}\hat{y}$ and $b = \hat{y}$ are the lattice vectors of 1×1 unit cell (black lines). In Fig. 4(b), we can see how the special k-points of general supercells (blues lines) are mapped onto those of 1×1 unit cell (black lines) in reciprocal space. In k-space, the length of supercell lattice vector is contracted by the factor,

$$\alpha = |a_{n,m}| = |b_{n,m}| = \sqrt{n^2 + nm + m^2}, \tag{1}$$

and the geometric condition $\overline{M_1K_1} \cdot N_s = \overline{M_2K}$ results in the integer value of N_s,

$$N_s = \frac{2}{\sqrt{3}}\alpha \cos\left(\frac{\pi}{6} - \theta\right) = n - m. \tag{2}$$

The location of special k-point K for a general hexagonal supercell is determined by the conditions,

$$\text{Mod}(N_s, 3) = \begin{cases} 0 & : \text{K} \to \Gamma \\ 1, 2 & : \text{K} \to \text{K}. \end{cases} \tag{3}$$

In striking contrast to graphene/MoS$_2$, the band offsets in Ti/MoS$_2$ show very insensitive behaviors to gate-voltages. To see the differences between graphene/MoS$_2$ and Ti/MoS$_2$, we constructed three different Ti/MoS$_2$ stacking configurations (T1, T2, and T3) as shown in Fig. 5(a–c). Among them, T1 configuration has the lowest total energy, but all the band structures of T1, T2, and T3 configurations are very similar to one another. Figure 5(f–h) show the band structures of T1 configuration. Distinct from graphene/MoS$_2$, Fig. 5(f) shows that Ti/MoS$_2$ has a strong band mixing along the Γ-M-K-Γ line in the energy range from -1.0 to 1.0 eV. This strong interaction is expected from a short equilibrium distance ~1.60 Å between Ti and MoS$_2$, which is less than half the distance ~3.23 Å between graphene and MoS$_2$. The binding energy between 2×2-Ti and 2×2-MoS$_2$ is found to be -8.32 eV, which indicates that Ti and MoS$_2$ stick together 14 times stronger than graphene and MoS$_2$. Comparing Fig. 5(f) with Fig. 5(g) and (h), we see that the position and the shape of Ti bands exhibit negligible
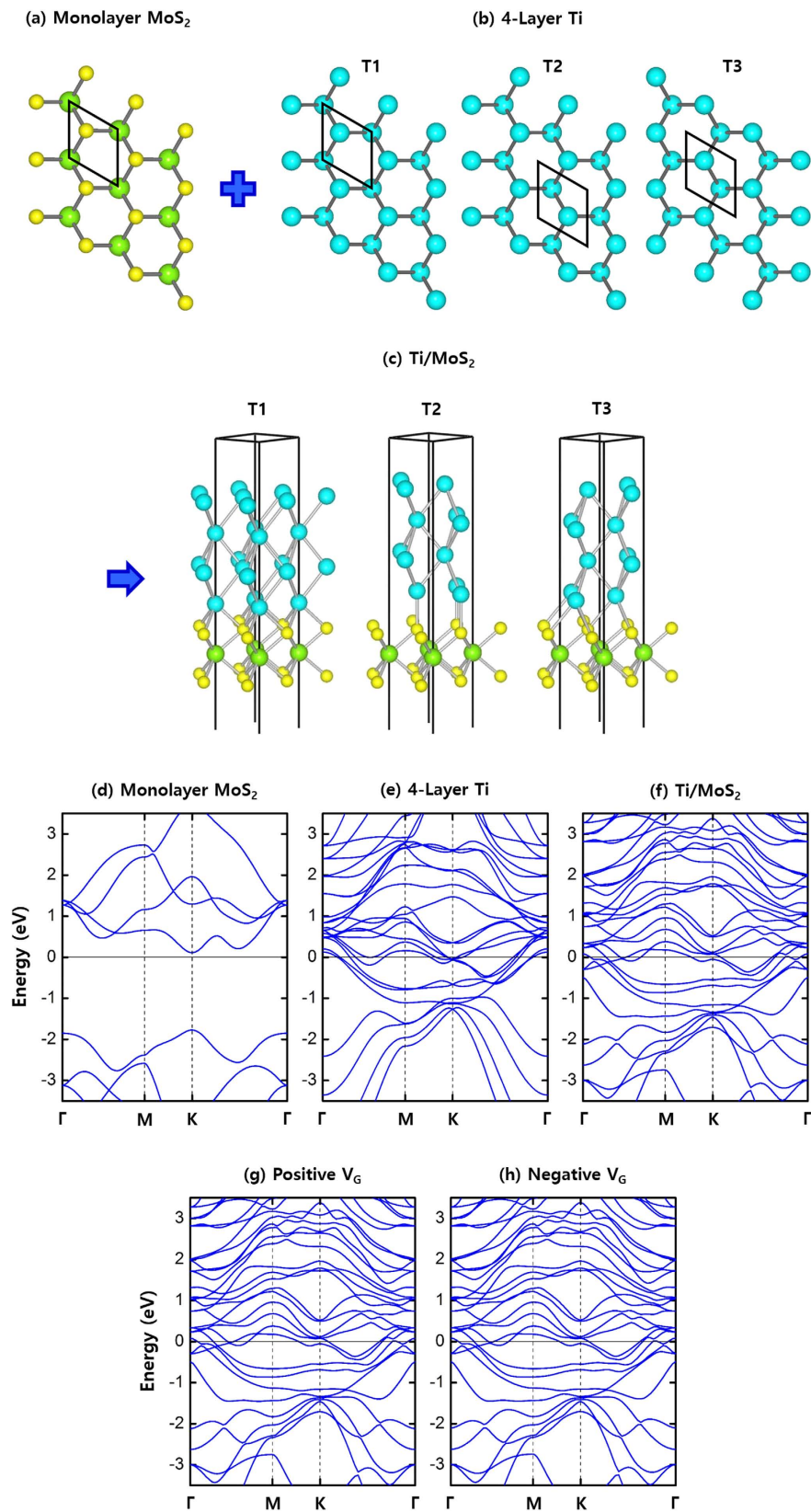
Figure 5. Atomic views and electronic band structures. (**a**) Top-view of monolayer MoS_2. (**b**) Top-views of 4-layer Ti slabs with three different origin choices, denoted as T1, T2, and T3. (**c**) Ti/MoS_2 heterostructures. (**d**) Band structure of 1×1 MoS_2 monolayer. (**e**) Band structure of 4-layer Ti. Band structures of Ti/MoS_2 in the T1 configuration (**f**) without the gate-voltage, (**g**) under a positive gate-voltage ($E = +0.01$ V/Å and $n_c = 8.7 \times 10^{12}$ cm^{-2}), and (**h**) under a negative gate-voltage ($E = -0.01$ V/Å and $n_c = -8.7 \times 10^{12}$ cm^{-2}). The direction of a positive electric field is from MoS_2 to Ti.

changes under V_G ($E = \pm 0.01$ V/Å and $n_c = \pm 8.7 \times 10^{12}$ cm^{-2}). Even when we increase the gate-voltages by 10 times ($E = \pm 0.1$ V/Å and $n_{ch} = \pm 8.7 \times 10^{13}$ cm^{-2}), the relative positions of Ti bands are not significantly altered from those in Fig. 5(g) and (h), implying that the intrinsic small Schottky barrier at the interface remains nearly constant without diminishing or rising under the strong gate-voltage. This insensitivity to the gate-voltage is also found in other ohmic metals such as Au (See Supplementary Information).

In conclusion, by simultaneous control of external electric fields and electron charging concentrations, we have compared the band offsets in graphene (S/D)-MoS$_2$ with those in Ti(S/D)-MoS$_2$. Under gate-voltages, the Dirac point positioning inside the MoS$_2$ bandgap is easily modulated with respect to the co-varying Fermi level, while the linearity of graphene bands remains intact around the Dirac point. Band lineups in graphene/MoS$_2$ explicitly confirms the absence of graphene-induced gap-states, which is thought to prevent the Fermi level pinning and preferably make graphene bands flexible. In contrast to Ti-MoS$_2$, graphene-MoS$_2$ interactions are very weak as evidenced from the small binding energy of -0.59 eV and the large equilibrium distance between graphene and MoS$_2$ ~3.23 Å, which is more than twice the equilibrium distance ~1.60 Å between Ti and MoS$_2$. In effect, the strong decoupling between graphene and MoS$_2$ bands causes a high sensitivity to gate-voltages. We respectively analyzed the fast increasing on-current and the steadily maintained (or lowered) off-current states, which originate from such a sensitive work function tuning of graphene under positive and negative V_G; such work function tuning, in sum, leads to the high on/off ratio in graphene/MoS$_2$.

References

1. Mak, K. F., Lee, C., Hone, J., Shan, J. & Heinz, T. F. Atomically thin MoS$_2$: a new direct-gap semiconductor. *Phys. Rev. Lett.* **105,** 136805 (2010).
2. Splendiani, A. *et al.* Emerging photoluminescence in monolayer MoS$_2$. *Nano Lett.* **10,** 1271–1275 (2010).
3. Geim, A. K. & Novoselov, K. S. The rise of graphene. *Nat. Mater.* **6,** 183–191 (2007).
4. Novoselov, K. S. *et al.* Electric field effect in atomically thin carbon films. *Science* **306,** 666–669 (2004).
5. Britnell, L. *et al.* Field-effect tunneling transistor based on vertical graphene heterostructures. *Science* **335,** 947–950 (2012).
6. Yang, H. *et al.* Graphene barristor, a triode device with a gate-controlled Schottky barrier. *Science* **336,** 1140–1143 (2012).
7. Dean, C. R. *et al.* Boron nitride substrates for high-quality graphene electronics. *Nat. Nanotechnol.* **5,** 722–726 (2010).
8. Yin, Z. *et al.* Memory devices using a mixture of MoS$_2$ and graphene oxide as the active layer. *Small* **9,** 727–731 (2013).
9. Bae, S. *et al.* Roll-to-roll production of 30-inch graphene films for transparent electrodes. *Nat. Nanotechnol.* **5,** 574–578 (2010).
10. Schwierz, F. Graphene transistors. *Nat. Nanotechnol.* **5,** 487–496 (2010).
11. Chhowalla, M. *et al.* The chemistry of two-dimensional layered transition metal dichalcogenide nanosheets. *Nat. Chem.* **5,** 263–275 (2013).
12. Ramasubramaniam, A., Naveh, D. & Towe, E. Tunable band gaps in bilayer transition-metal dichalcogenides. *Phys. Rev. B* **84,** 205325 (2011).
13. Liu, Q. *et al.* Tuning electronic structure of bilayer MoS$_2$ by vertical electric field: a first-principles investigation. *J. Phys. Chem. C* **116,** 21556–21562 (2012).
14. Yue, Q. *et al.* Bandgap tuning in armchair MoS$_2$ nanoribbon. *J. Phys.: Conden. Matter* **24,** 335501 (2012).
15. Johari, P. & Shenoy, V. B. Tuning the electronic properties of semiconducting transition metal dichalcogenides by applying mechanical strains. *ACS Nano* **6,** 5449–5456 (2012).
16. Ohta, T., Bostwick, A., Seyller, T., Horn, K. & Rotenberg, E. Controlling the electronic structure of bilayer graphene. *Science* **313,** 951–954 (2006).
17. Latil, S. & Henrard, L. Charge carriers in few-layer graphene films. *Phys. Rev. Lett.* **97,** 036803 (2006).
18. Castro, E. V. *et al.* Biased bilayer graphene: semiconductor with a gap tunable by the electric field effect. *Phys. Rev. Lett.* **99,** 216802 (2007).
19. Zhang, L. M. *et al.* Determination of the electronic structure of bilayer graphene from infrared spectroscopy. *Phys. Rev. B* **78,** 235408 (2008).
20. Chang, K. & Chen, W. *In situ* synthesis of MoS$_2$/graphene nanosheet composites with extraordinarily high electrochemical performance for lithium ion batteries. *Chem. Commun.* **47,** 4252–4254 (2011).
21. Li, Y. *et al.* MoS$_2$ nanoparticles grown on graphene: an advanced catalyst for the hydrogen evolution reaction. *J. Am. Chem. Soc.* **133,** 7296–7299 (2011).
22. Shi, Y. *et al.* van der Waals epitaxy of MoS$_2$ layers using graphene as growth templates. *Nano Lett.* **12,** 2784–2791 (2012).
23. Lee, Y.-H. *et al.* Synthesis and transfer of single-layer transition metal disulfides on diverse surfaces. *Nano Lett.* **13,** 1852–1857 (2013).
24. Ma, Y., Dai, Y., Guo, M., Niu, C. & Huang, B. Graphene adhesion on MoS$_2$ monolayer: an ab initio study. *Nanoscale* **3,** 3883–3887 (2011).
25. Miwa, R. H. & Scopel, W. L. Lithium incorporation at the MoS$_2$/graphene interface: an ab initio investigation. *J. Phys.: Conden. Matter* **25,** 445301 (2013).
26. Britnell, L. *et al.* Strong light-matter interactions in heterostructures of atomically thin films. *Science* **340,** 1311–1314 (2013).
27. Yu, W. J. *et al.* Vertically stacked multi-heterostructures of layered materials for logic transistors and complementary inverters. *Nat. Mater.* **12,** 246–252 (2013).
28. Choi, M. S. *et al.* Controlled charge trapping by molybdenum disulphide and graphene in ultrathin heterostructured memory devices. *Nat. Commun.* **4,** 1624 (2013).
29. Lee, Y. T. *et al.* Graphene versus ohmic metal as source-drain electrode for MoS$_2$ nanosheet transistor channel. *Small* **10,** 2356–2361 (2014).
30. Yuchen, D. *et al.* MoS$_2$ field-effect transistors with graphene/metal heterocontacts. *Electron Device Lett., IEEE* **35,** 599–601 (2014).
31. Lu, C.-P., Li, G., Watanabe, K., Taniguchi, T. & Andrei, E. Y. MoS$_2$: choice substrate for accessing and tuning the electronic properties of graphene. *Phys. Rev. Lett.* **113,** 156804 (2014).
32. Yoon, J. *et al.* Highly flexible and transparent multilayer MoS$_2$ transistors with graphene electrodes. *Small* **9,** 3295–3300 (2013).
33. Shih, C.-J. *et al.* Tuning on–off current ratio and field-effect mobility in a MoS$_2$–graphene heterostructure via Schottky barrier modulation. *ACS Nano* **8,** 5790–5798 (2014).
34. Tian, H. *et al.* Novel field-effect Schottky barrier transistors based on graphene-MoS$_2$ heterojunctions. *Sci. Rep.* **4** (2014).
35. Kwak, J. Y. *et al.* Electrical characteristics of multilayer MoS$_2$ FET's with MoS$_2$/graphene heterojunction contacts. *Nano Lett.* **14,** 4511–4516 (2014).
36. Bertolazzi, S., Krasnozhon, D. & Kis, A. Nonvolatile memory cells based on MoS$_2$/graphene heterostructures. *ACS Nano* **7,** 3246–3252 (2013).
37. Yu, L. *et al.* Graphene/MoS$_2$ hybrid technology for large-scale two-dimensional electronics. *Nano Lett.* **14,** 3055–3063 (2014).

38. Jin, C., Rasmussen, F. A. & Thygesen, K. S. Tuning the Schottky Barrier at the Graphene/MoS₂ Interface by Electron Doping: Density Functional Theory and Many-Body Calculations. *J. Phys. Chem. C* **119**, 19928–19933 (2015).
39. Liu, B. *et al.* First-principles investigation of the Schottky contact for the two-dimensional MoS₂ and graphene heterostructure. *RSC Adv*. **6**, 60271–60276 (2016).
40. Kim, S. *et al.* High-mobility and low-power thin-film transistors based on multilayer MoS₂ crystals. *Nat. Commun.* **3**, 1011 (2012).
41. Late, D. J., Liu, B., Matte, H. S. S. R., Dravid, V. P. & Rao, C. N. R. Hysteresis in single-layer MoS₂ field effect transistors. *ACS Nano* **6**, 5635–5641 (2012).
42. Das, S., Chen, H.-Y., Penumatcha, A. V. & Appenzeller, J. High performance multilayer MoS₂ transistors with scandium contacts. *Nano Lett.* **13**, 100–105 (2012).
43. Das, S. & Appenzeller, J. Screening and interlayer coupling in multilayer MoS₂. *Phys. Status Solidi – Rapid Research Letters* **7**, 268–273 (2013).
44. Buscema, M. *et al.* Large and tunable photothermoelectric effect in single-layer MoS₂. *Nano Lett.* **13**, 358–363 (2013).
45. Radisavljevic, B., Whitwick, M. B. & Kis, A. Integrated circuits and logic operations based on single-layer MoS₂. *ACS Nano* **5**, 9934–9938 (2011).
46. Lee, H. S. *et al.* MoS₂ nanosheet phototransistors with thickness-modulated optical energy gap. *Nano Lett.* **12**, 3695–3700 (2012).
47. Lembke, D. & Kis, A. Breakdown of high-performance monolayer MoS₂ transistors. *ACS Nano* **6**, 10070–10075 (2012).
48. Van der Zande, A. M. *et al.* Grains and grain boundaries in highly crystalline monolayer molybdenum disulphide. *Nat. Mater.* **12**, 554–561 (2013).
49. Lopez-Sanchez, O., Lembke, D., Kayci, M., Radenovic, A. & Kis, A. Ultrasensitive photodetectors based on monolayer MoS₂. *Nat. Nanotechnol.* **8**, 497–501 (2013).
50. Radisavljevic, B. & Kis, A. Mobility engineering and a metal–insulator transition in monolayer MoS₂. *Nat. Mater.* **12**, 815–820 (2013).
51. Schottky, W. Zur Halbleitertheorie der sperrschicht- und spitzengleichrichter. *Zeitschrift für Physik* **113**, 367–414 (1939).
52. Mott, N. F. The theory of crystal rectifiers. *Proc. R. Soc. Lond. A* **171**, 27 (1939).
53. Tung, R. T. The physics and chemistry of the Schottky barrier height. *Appl. Phys. Rev*. **1**, 011304 (2014).
54. Soler, J. M. *et al.* The SIESTA method for ab initio order-N materials simulation. *J. Phys.: Conden. Matter* **14**, 2745 (2002).
55. Leonard, F. & Talin, A. A. Electrical contacts to one- and two-dimensional nanomaterials. *Nat. Nanotechnol*. **6**, 773–783 (2011).
56. Perdew, J. P. & Zunger, A. Self-interaction correction to density-functional approximations for many-electron systems. *Phys. Rev. B* **23**, 5048–5079 (1981).
57. Troullier, N. & Martins, J. L. Efficient pseudopotentials for plane-wave calculations. *Phys. Rev. B* **43**, 1993–2006 (1991).
58. Kleinman, L. & Bylander, D. M. Efficacious form for model pseudopotentials. *Phys. Rev. Lett.* **48**, 1425–1428 (1982).
59. Fivaz, R. & Mooser, E. Mobility of charge carriers in semiconducting layer structures. *Phys. Rev.* **163**, 743–755 (1967).
60. Bichsel, R. & Levy, F. Influence of process conditions on the electrical and optical properties of RF magnetron sputtered MoS₂ films. *J. Phys. D: Appl. Phys.* **19**, 1809 (1986).
61. Dave, M., Vaidya, R., Patel, S. G. & Jani, A. R. High pressure effect on MoS₂ and MoSe₂ single crystals grown by CVT method. *Bull. Mater. Sci.* **27**, 213–216 (2004).
62. Lee, K. *et al.* Electrical characteristics of molybdenum disulfide flakes produced by liquid exfoliation. *Adv. Mater.* **23**, 4178–4182 (2011).

Acknowledgements

Author Contributions

S.S.B. wrote the manuscript, performed first-principles calculations, and formulated analytic equations. S.I. and H.J.C. partly wrote the manuscript. All authors analyzed the data and reviewed the manuscript.

Additional Information

Supplementary information accompanies this paper at http://www.nature.com/srep

Competing Interests: The authors declare no competing financial interests.

How to cite this article: Baik, S. S. *et al.* Work Function Tuning in Two-Dimensional MoS₂ Field-Effect-Transistors with Graphene and Titanium Source-Drain Contacts. *Sci. Rep.* **7**, 45546; doi: 10.1038/srep45546 (2017).

Publisher's note: Springer Nature remains neutral with regard to jurisdictional claims in published maps and institutional affiliations.